ARTICLE TEXT for

CAST ALUMINIUM SINGLE CRYSTALS CROSS THE THRESHOLD FROM BULK TO SIZE-DEPENDENT STOCHASTIC PLASTICITY

J. Krebs*, S.I. Rao**, S. Verheyden, C. Miko, R. Goodall, W.A. Curtin and A. Mortensen

*Corresponding author for experiments, ** Corresponding author for simulations

Ecole Polytechnique Fédérale de Lausanne (EPFL); Lausanne CH-1015 Switzerland

ABSTRACT

Metals are known to exhibit mechanical behaviour at the nanoscale different to bulk samples. This transition typically initiates at the micron-scale, yet existing techniques to produce micron-sized samples often introduce artefacts that can influence deformation mechanisms. Here, we demonstrate the casting of micron-scale aluminium single crystal wires by infiltration of a salt mould. Samples have millimetre lengths, smooth surfaces, a range of crystallographic orientations, and a diameter D as small as 6 µm. The wires deform in bursts, at a stress that increases with decreasing D. Bursts greater than 200 nm account for roughly 50% of wire deformation and have exponentially distributed intensities. Dislocation dynamics simulations show that single-arm sources that produce large displacement bursts halted by stochastic cross-slip and lock formation explain microcast wire behaviour. This microcasting technique may be extended to several other metals or alloys and offers the possibility of exploring mechanical behaviour spanning the micron-scale.

MAIN ARTICLE TEXT

There is a transition in the plastic deformation of metallic samples as their size falls below 10 to 100 μm: as the sample size decreases, its flow stress increases sharply and the progression of plastic deformation is no longer smooth, proceeding instead in bursts that often show scaling characteristics of self-organized criticality (recent reviews are in Refs. [1-6]). Understanding this transition from macro- to microplasticity has been a long-lasting challenge, in part because most small-scale metal samples are fabricated using processes completely different from those used when making samples of bulk metal. Typically, micron-range samples of metal for mechanical testing are made using either (i) thin-film deposition methods, which generally produce metals having small grains and a high defect population, (ii) Focused Ion Beam (FIB) micromilling, which introduces a layer of irradiated, gallium-implanted material along the sample surface [7-11], or (iii) selective dissolution [12, 13, 14]. Each of these methods has its advantages, but none straddles the wide range of sizes across which one sees the transition from small-scale to bulk plasticity.

Here, we show how the age-old process of metal casting can be made to cross the gap from macro to micro sample sizes. We show that aluminium can be cast into tiny moulds to produce single-crystalline wires of high geometric perfection having a diameter D as small as 6 μm and lengths of ~1 mm, far longer than can be achieved with conventional microsamples. Tension tests on these microcast wires display a size effect in flow stress, show a transition to burst-like "crackling" deformation and also, by virtue of their exceptional aspect ratio, yield extensive data on the statistical distribution of slip bursts up to sizes one order of magnitude larger than those seen in micropillars (up to 1 μm vs. up to 100 nm). The smaller cast microcrystals furthermore meet the upper limit of what can nowadays be simulated using large-scale 3D Discrete Dislocation ("DD") codes, where individual dislocations and their movement are directly simulated [1,2,15]. DD simulations "at scale" agree quantitatively and qualitatively with data collected in the microwires,

2

which in turn enables the identification of mechanisms that explain the observed wire deformation behaviour.

The state of the art in microcasting uses polycrystalline moulds of ceramic or plaster [16,17]. This produces metallic specimens a little under a millimetre wide, which is above the threshold for probing small-scale plasticity. We push here the state-of-the-art and demonstrate production of what are, to our knowledge, the smallest shaped aluminium castings in the world. Achieving precision casting at the micron scale required that some physical barriers be overcome. First, metals do not wet most mould materials and have high surface tensions; this prevents the spontaneous flow of molten metal into very small mould cavities. Second, the mould material must be shaped to high precision and must be easy to separate from the fragile microcasting. Figure 1 illustrates the process; details are given in the Methods section and the Supplementary Information (SI). To overcome capillary forces, we pressurize the metal. We use shaped single-crystalline moulds because, at the microscale, any grain boundary along the mould wall will groove during heat-up, producing a sizeable surface defect on the casting. Our moulds are made by growing NaCl single crystals around an organic fibre. After drying and then heating in air to pyrolize the fibre, one obtains NaCl single-crystals containing a hollow having the shape of the fibre, which is then infiltrated with pressurized molten aluminium. Once solidified, the metal is gently freed from the mould by dissolution in water. This creates cast aluminium microwires that are monocrystalline, pore-free, smooth to within a few tens of nanometres, one to three millimetre long, and that have a tailored diameter D between 6 and 100 µm, Figs. 1c-e.

A few castings were observed in the Transmission Electron Microscope (TEM), see the SI. The initial dislocation density is around 1.2×10^{11} m^{-2} and 1.4×10^{12} m^{-2} in a FIB-milled TEM lamellae produced from 15 µm and 7 µm diameter wires, respectively. These values are not very precise, since FIB-milling had to be used to extract thin sections of the wires; the important point is that they are low and typical of annealed bulk metal.
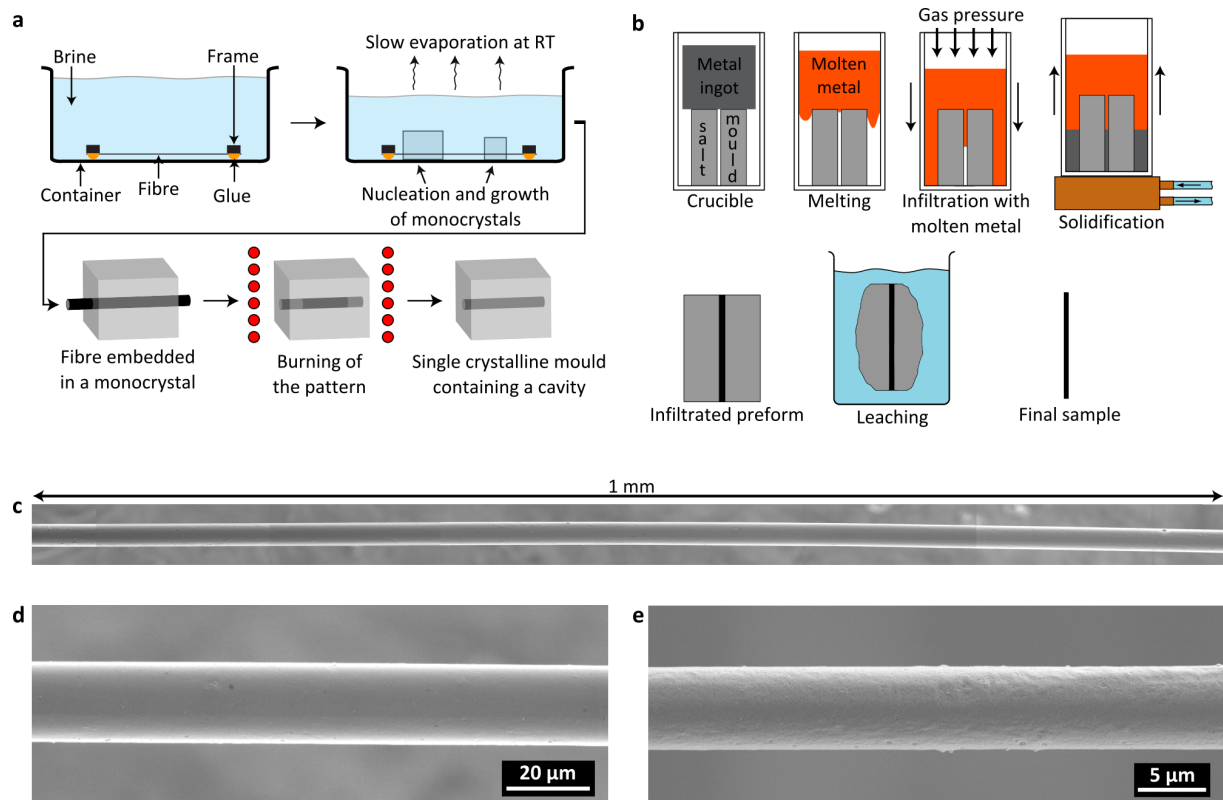
Figure 1.Casting process and resulting cast wires. (**a**) Illustration showing the crystallization of single crystals of sodium chloride around pyrolysable fibres that are then burnt in order to prepare microcasting moulds. (**b**) Illustration representing the different casting steps for the casting of an aluminium wire with diameter in the micrometre range. (**c-e**) SEM images of 99.99% purity aluminium wires with a diameter of 19 μm (**c & d**) and 6.2 μm (**e**) produced by the microcasting process illustrated in (**a & b**). Each of these wires is more than 1000 μm, generally 2000 μm, long.

Given their high aspect ratio, the wires are amenable to tensile testing. Tensile tests were conducted at room temperature and at a displacement rate of 300 nm/s, see Methods. Force and wire elongation measurements were collected at 50 kHz and 50 Hz respectively; the high sampling rate for the force data permits detection and measurement of sudden load drops observed during the test (see Methods and SI). All wires were tested up to tensile failure.
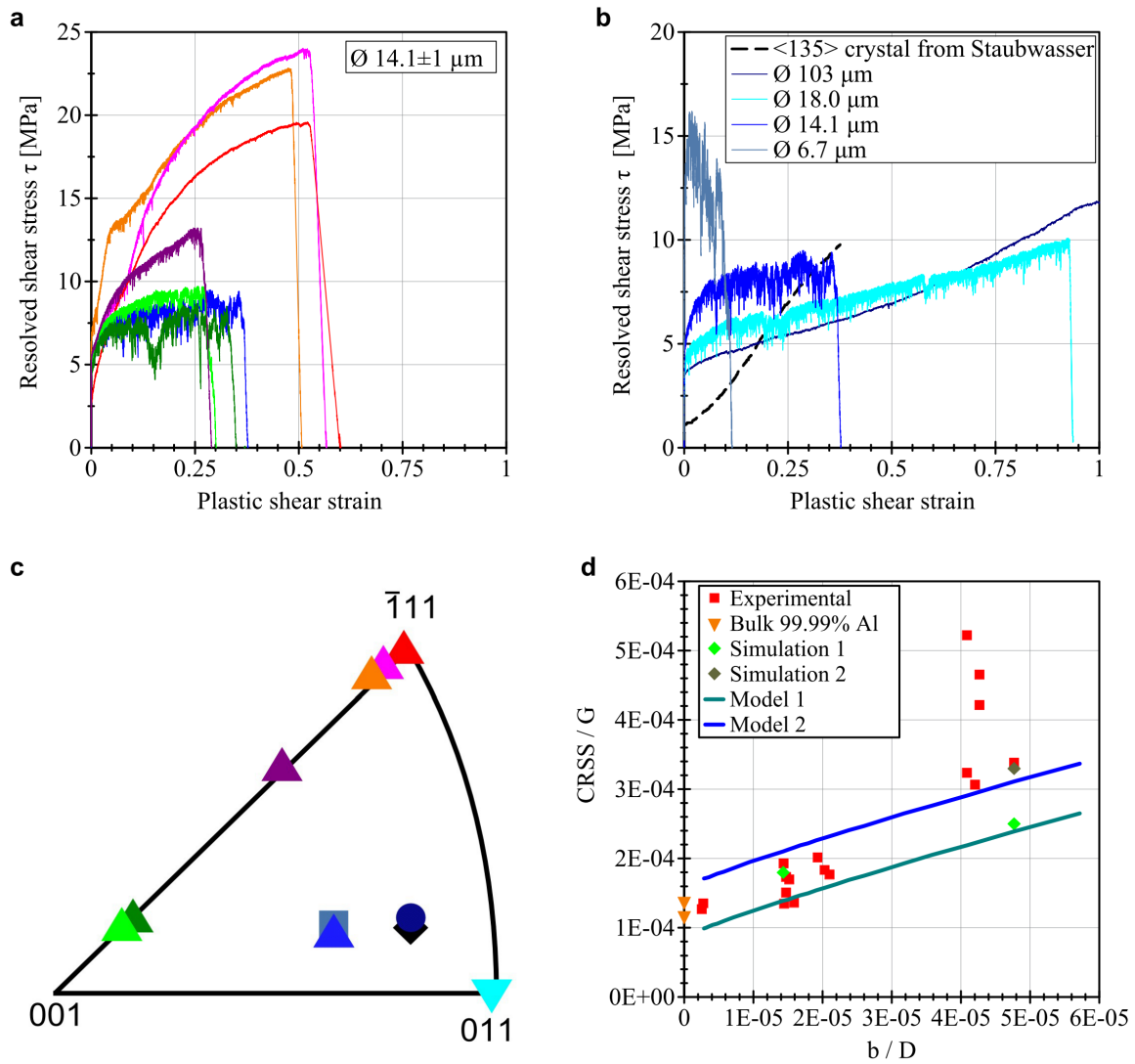
Figure 2. Microcast aluminium tensile curves and the size effect. (**a**) Resolved shear stress versus resolved plastic shear strain for wires with a diameter *D* in the range between 13 and 16 µm (see Supplementary On-Line Material Section for a collection of all data); (**b**) Curves of resolved shear stress versus resolved plastic shear strain for wires initially oriented for single slip but with *D* going from 100 µm down to 7 µm together with a curve in the literature for macroscopic crystals [29]. (**c**) Standard stereographic triangle showing the crystallographic orientation of the tested wires in (a) and (b); (**d**) plot of the measured Critical Resolved Shear Stress (CRSS) at 0.2% plastic shear strain normalized by the shear modulus *G* (red points) versus the inverse of *D* normalized by the Burgers vector *b* for all tested wires except those with an initial orientation near <111> (for which data were only obtained for a single wire diameter), together with corresponding predictions from 3D dislocation dynamics simulations and the analytical single-arm source model. Simulation 1 and Model 1 assume a total initial dislocation density of $6 \times 10^{11}/m^2$, whereas Simulation 2 and Model 2, assume a total initial dislocation density of $\sim 2 \times 10^{12}/m^2$ (more information in the SI). On the same plot, the critical resolved shear stress of the bulk aluminium used to cast the microwires, from tensile tests conducted on cast macroscopic tensile samples, is also shown (orange inverted triangles).

Figure 2 shows a representative portion of tensile test results (the entire set of data is given in the

SI). It is apparent that the flow curves vary both with orientation, Fig. 2a, and with *D*, Fig. 2b.

The dependence on crystal orientation is strong: the global work hardening rate decreases as the number of active stable slip systems decreases from three (wire axis ~ <111>) to two (wire axis ~ <112>) to one (all other orientations including <011>). As the number of stable glide systems decreases, the flow curve also becomes increasingly serrated, displaying sudden stochastically distributed displacement jumps, manifest as sudden decreases in stress. Large displacement jumps essentially disappear, giving nearly smooth stress-strain curves when 13 or 14 μm wires are oriented along the <111> direction, where three slip systems operate simultaneously [1].

The increase in flow stress with decreasing D, Fig. 2d, is proof that the "plasticity size effect" is manifest in these castings. At small D the flow stress varies strongly from sample to sample; collating the data shows that (within the significant scatter) the flow stress increases as $1/D$ for 6 μm ≤ D ≤ 100 μm, consistent with data for drawn, annealed and leached bamboo-structure aluminium wires [18], for aluminium micropillars [19], and for submicrometre (copper-containing) primary α-aluminium crystals leached from the Al-Al$_2$Cu eutectic [12].

The dependence of strength on diameter and orientation suggests that, at $D \approx 20$ μm and below, the deformation of aluminium single crystals is driven by the activation of dislocation sources the sizes of which scale with D. Large-scale 3D dislocation dynamics simulations [1,2,15], with thermally-activated cross-slip included [15,20,21] (see Methods and SI) of uniaxial tension of aluminium wires having dimensions 6 x 6 x 50 and 20 x 20 x 50 μm^3 (i.e. D = 6, 20 μm) for the <111>, <001>, and <110> orientations yield the normalized shear-stress/shear-strain curves shown in Fig. 3 under displacement control Fig. 3(a&b) and load control Fig. 3(c&d). All three orientations show roughly similar initial flow stresses at each diameter, with a higher hardening rate (over the small range of strain simulated) for the multislip <111> and <001> orientations, as compared to the single-slip <110> orientation. The predicted flow stress increases from D = 20 μm to D = 6 μm, and the magnitude of the increase is consistent with the experimental data (see Fig. 2d), albeit falling in the lower range of measured values. At D=6 μm there is also significant scatter in the simulation results,

associated with variations in initial dislocation distribution. This is consistent with, and rationalizes, the scatter observed experimentally in the flow stress at *D*=6 μm. The DD simulations thus reproduce the trends observed experimentally.

The 0.2% yield stress in the DD simulations is governed by the operation of single-arm-sources moving through a forest created by the expansion of the initial Frank-Read sources (of strengths 0.75 – 2.23 MPa [20], see Movies in SI). The 1/D scaling of strength is consistent with analytical models of single-arm-source operation.
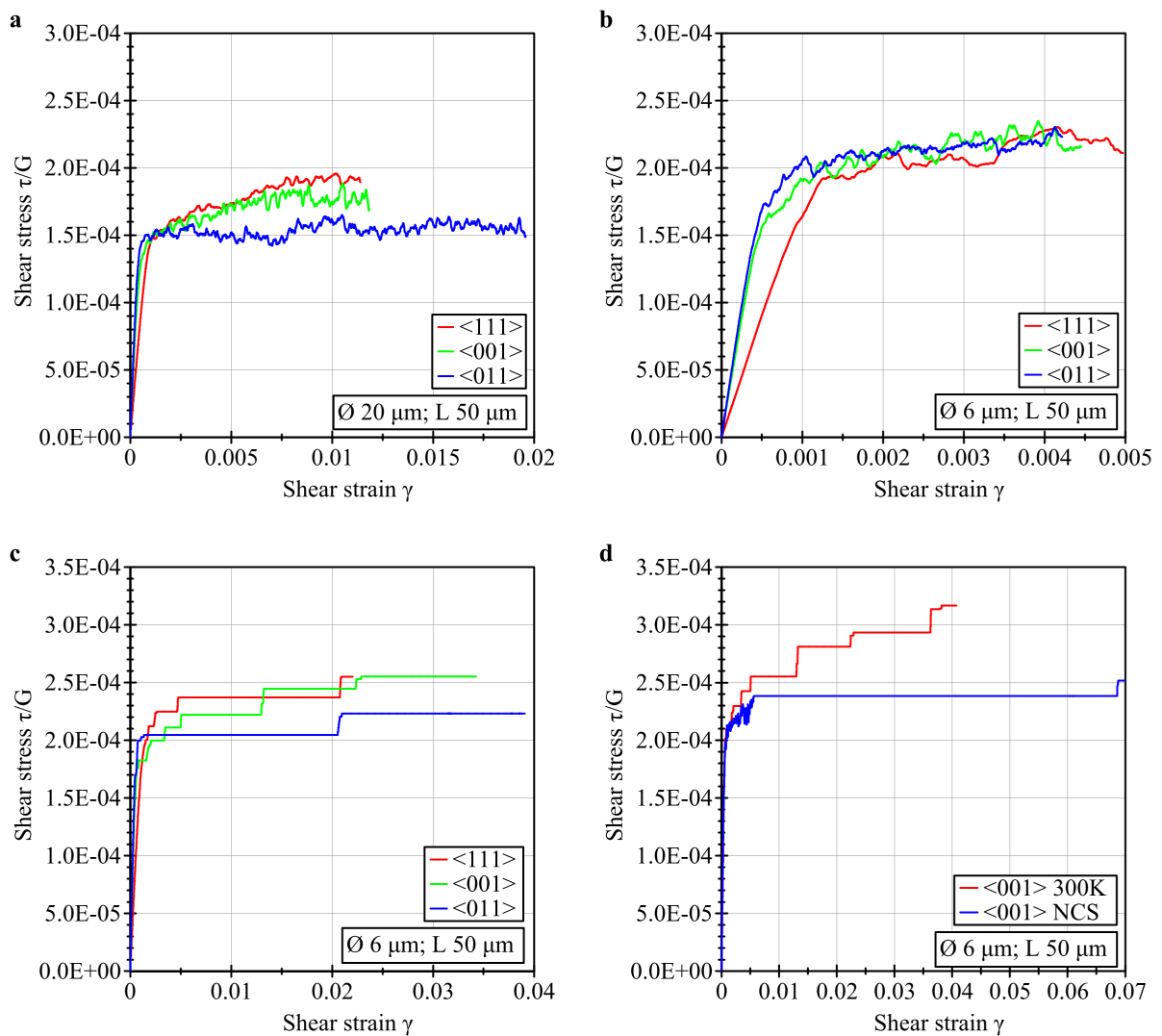

Figure 3: Simulated tensile curves in resolved coordinates. Resolved shear stress vs resolved shear strain curves obtained from 3D dislocation dynamics simulations accounting for thermally activated cross-slip in (**a**) 20 x 20 x 50 μm^3 and (**b**) 6 x 6 x 50 μm^3 domains in displacement control, (**c**) in 6 x 6 x 50 μm^3 domain in load control, and (**d**) 6 x 6 x 50 μm^3, (001) orientation, 300K cross-slip (under load control) and no cross-slip (under displacement control up to a shear strain of 0.005, and from that point onwards under load control). The simulations were performed assuming an initial total dislocation density of ~ 6 × 10^{11}/m^2.
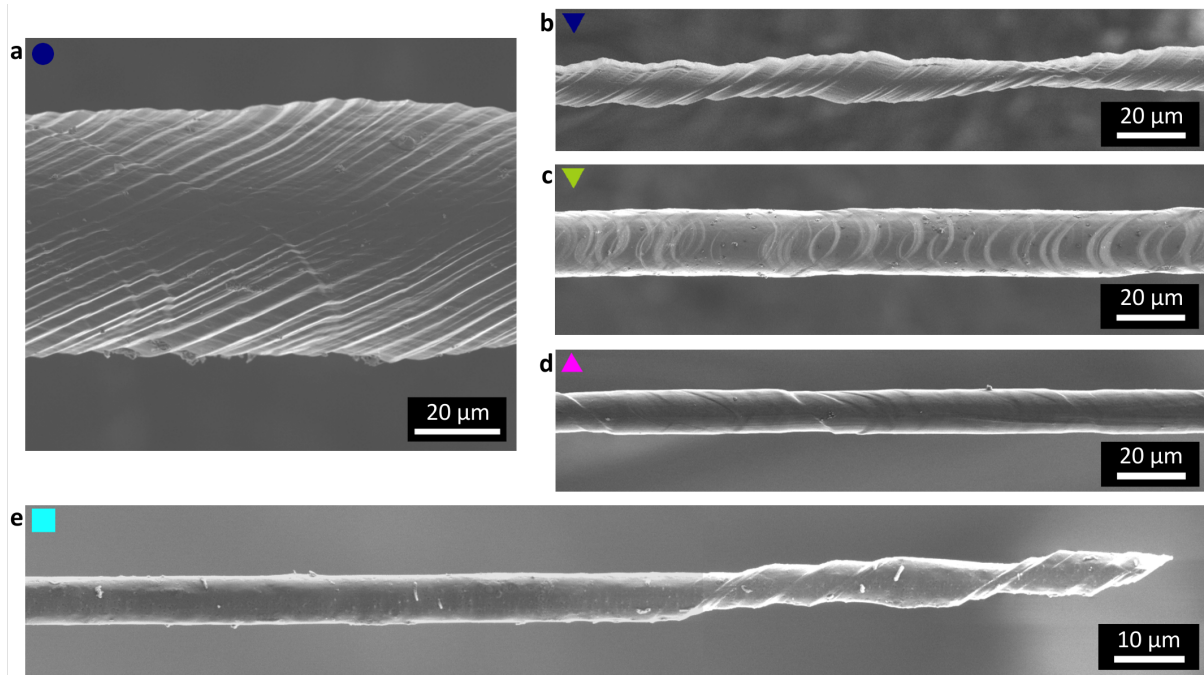
Figure 4. Slip steps on deformed cast Al microwires. SEM images of the wire surface topography after tensile testing. (**a**) 110 µm diameter wire with slip traces along mainly one glide system; (**b**) 19 µm diameter wire with an <110> initial crystallographic orientation deformed by shear along 1 glide system; (**c**) when the initial orientation approaches the <001>-<111> boundary line, slip steps from a second glide system become more and more pronounced, until both systems are equally distributed when the sample direction is along that line (as is the case for this sample); (**d**) 15 µm diameter microwire with a crystallographic orientation close to the <111> corner: such wires exhibit few and small slip steps coming from two or three different glide systems; (**e**) a 7 µm diameter wire that failed below 10% plastic strain; it deformed by glide along mainly one system and then failed by highly localized slip at one location (small colour symbols are to guide the reader when consulting the full collection of data in the Supplementary On-Line Material).

The most interesting feature of the present data (Figs. 2a,b) is that, as D decreases and for wires oriented such that one or two slip systems are activated, the deformation proceeds via increasingly dominant sudden plastic flow bursts. Similar intermittent, burst-like, deformation was observed with FIB-machined samples in compression (e.g.[22])) or tension (e.g. [23]); however, the microcast aluminium crystals are free of ion-milling damage and are far longer, such that clean tensile data are produced, free of end effects and sampling many more, and far larger, displacement bursts than can be obtained with FIB-milled samples. The intermittent character of slip in microcast aluminium wires is reflected in their shape after deformation, Fig. 4: thicker wires ($D \approx 100$ µm, Fig. 4a) show regular and uniformly distributed slip steps while smaller wires ($D \leq 20$ µm, Fig. 4b) have more irregularly distributed slip steps. At fixed D, the slip step number and height decrease for wires oriented for

multiple slip (Figs. 4c,d). In the smallest wires, slip steps become so irregular that failure can suddenly occur if glide along one plane goes too far (Fig. 4e).

As seen in Fig. 3, the DD simulations reproduce the displacement bursts observed in experiments, especially under load control (Fig. 3c), which approximates the experimental loading better than does displacement control (see SI). Figure 3c shows three important features: (i) the simulated displacement bursts can be large (note that, when bursts are computed into strain, the smaller size of the simulated domains amplifies the size of bursts compared to experimental wire data), (ii) the displacement bursts eventually stop even when the stress is held constant (Figs. 3c&d) and (iii) the displacement bursts are larger in the single-slip orientation (~0.5 µm) as compared to multi-slip orientations (~0.1 µm). Examination of the simulated dislocation evolution (see Movies in SI) shows that these large plastic displacement bursts are due to the operation of only a few independent single-arm sources that operate continuously for many (100's) of revolutions through the surrounding forest; this will have important consequences for interpreting the displacement burst statistics (see below). DD simulations thus mechanistically rationalize key features of the observed deformation.
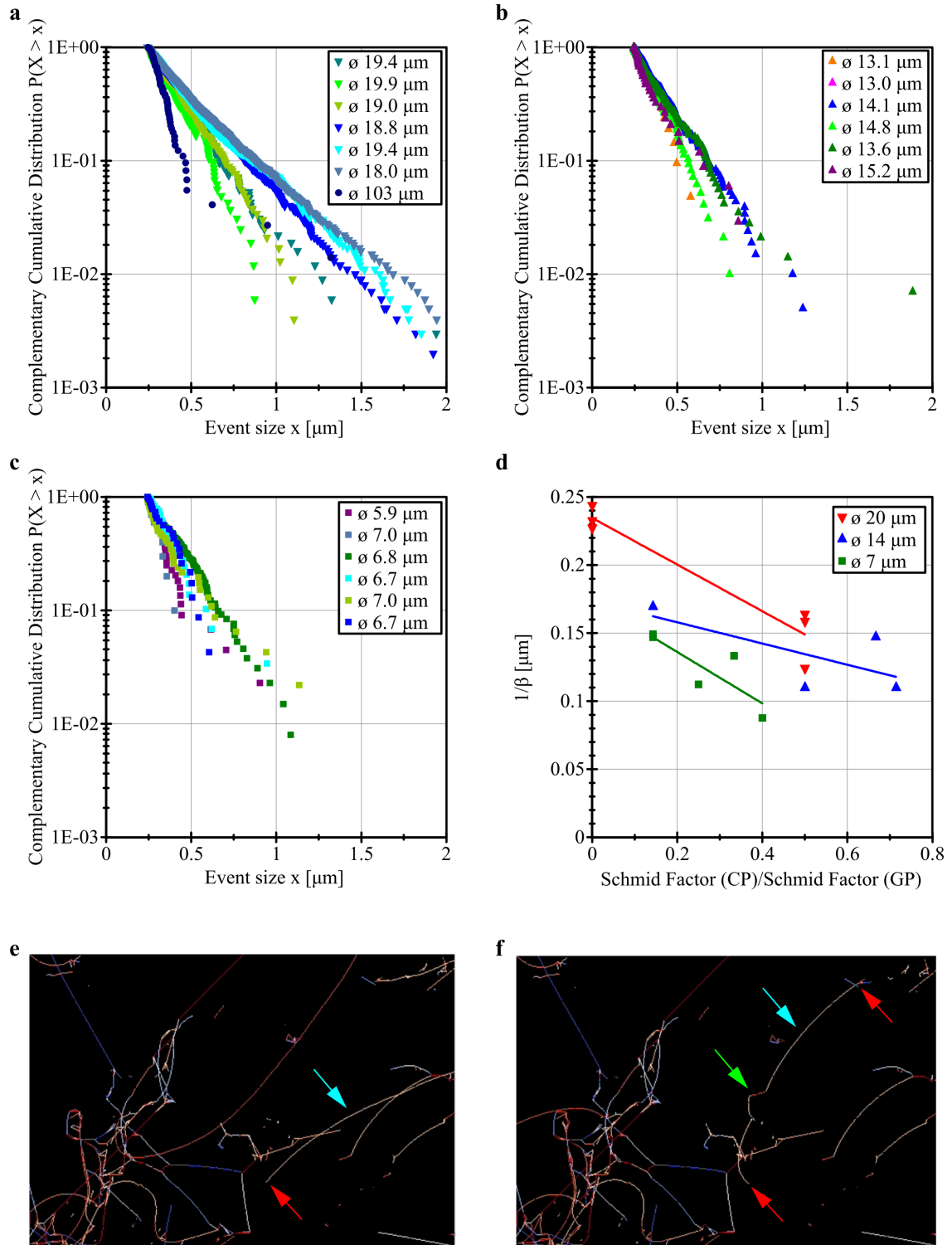
Figure 5. Displacement bursts: size distributions and underlying mechanisms. Complementary cumulative distribution function of larger displacement burst sizes, with event size expressed in terms of slip distance along the glide direction: distribution of data in (**a**) the 18-20 μm, (**b**) 13-15 μm and (**c**) 6-7 μm diameter wires plotted in semi-logarithmic coordinates (experimental data collected across all event size scales and plotted in log-log coordinates are given in the SI); (**d**) plot of β^{-1} versus the ratio of Schmid factor on the cross-slip plane to that on the glide plane for wires in the three size ranges explored here; (**e**) single-arm source stoppage captured by DD simulation in a 6 μm wide <001> orientation crystal at t = 32s: a rotating one-armed dislocation source (see blue arrow) pinned at one extremity (see red arrow) has generated extensive slip while cross-slipping continually then, at t = 33s (**f**), it stops concomitant with formation of a second pinning point (second, right-hand, red arrow) and a short segment on the cross-slip plane along the arm length (green arrow; see film in Supplementary Information for a better and more complete view of the dynamics).

With their very high aspect ratio, tensile tests on the microcast Al crystals give statistically significant numbers of large-amplitude displacement bursts. To measure the amplitude distributions, load-time data were collected at high frequency and were then treated to extract unambiguous load drops along the curves for all samples reported here (see Methods and SI). A simple analysis of the local average stress variation during each burst (see SI, Eq. S-8) shows that the decrease in stress driving dislocation activity during the bursts is relatively low.

Recorded stress drops were converted into shear displacements. The resolution of our apparatus allowed for the unambiguous detection of load drops of 75 µN or higher, corresponding to sudden slip displacement events of amplitude above a sample-dependent value below 200 nm. Summing these measured larger displacement bursts shows that the total strain due to these many larger events corresponds to ~40-50% of the total plastic strain in wires with $D \leq 20$ µm oriented for easy glide. In other words, detected displacement bursts are an essential element of the stress-strain behaviour of the wires.

The complementary cumulative distribution function of displacement burst sizes x is shown in Fig. 5a-c for wire diameters 18-100 µm, 13-15 µm and 7 µm, respectively, in semi-logarithmic form, plotting in Fig. 5 data for displacement amplitudes above 200 nm (for uniformity in the plots). As seen the large-amplitude burst distributions follow an exponential behaviour:

$$P(X > x) = e^{(\beta x_{\min})} \cdot e^{(-\beta x)} \quad (x > x_{\min}) \qquad \text{Eq. 1}$$

where $x_{\min} = b\, N_{\min}$ is the lowest recorded event size in the plots and β^{-1} is the characteristic burst size. Thus, the large-amplitude displacement bursts measured in microcast samples do not exhibit a power law or Gaussian distribution. Evidence for power-law scaling [19,22,24-28] can on the other hand be detected if one relaxes conditions on computed burst size to count all detected events; see the SI, Fig. S-10.

Deviations from power-law scaling that arise at larger burst size amplitudes, corresponding to a "cut-off" regime in measured or simulated burst distributions [2,24,25,27,28], have been attributed to driving stress variations during the burst. Specifically, using Eq. (9) of Ref. [31] with observed work hardening rates and load train compliance values (see the SI), one finds that the predicted cut-off of the burst size distribution is on the order of approximately one micrometre. The theory of "avalanche" dislocation bursts thus agrees with the present data in predicting the right order of magnitude for the observed maximum burst size values; however, the present data display an exponential distribution, different from the Gaussian-like distribution predicted near the cut-off by the analysis in Refs. [24,31].

Figure 5d plots measured values of β^{-1} in all microcast wires oriented for single slip versus the ratio of Schmid factor on the cross-slip plane to that on the glide plane, for each of the three ranges of D: ≈ 20 μm, ≈ 14 μm and ≈ 6 μm. As seen, β^{-1} decreases as this ratio increases. Its variation with D does not exceed scatter in the data (if anything, data give hints that there is a slight decrease in mean burst size with decreasing D; this might in part be due to the somewhat higher rate of decrease of the applied stress during the burst at small D, see SI Eq. S-8).

The DD simulations show that large plastic bursts correspond to the independent operation of single-arm-sources rotating many times across the sample before stopping. These sources are independent, and if their stopping is a random stochastic event then both the probability distribution and the cumulative probability distribution are exponential, as seen experimentally (Fig. 4). The burst size x corresponds to $x=Nb$, where b is the Burgers vector amplitude and N is the number of times the single-arm-source operates across the sample; β^{-1} then corresponds to a characteristic number of times $\overline{N}$ that a single-arm-source operates before stopping: $\overline{N} = \beta^{-1}/b$, and $e^{-\beta b}$ is the probability that the source remains active after one more sweep across the glide plane over an area spanning the wire cross-section. Data show 4 μm^{-1} < β < 9 μm^{-1}, and hence a typical burst size of 0.11 μm < $\overline{N}b$ < 0.25 μm corresponding to 300 < $\overline{N}$ < 900 operations of a single-arm-source prior to it

stopping. This level of single-arm-source operation is consistent with the DD simulations (see full cell [100] and [110] movies in the SI).

The major remaining question is "what stochastic event causes a triggered arm source to stop?" A first mechanism is the fact that the applied stress decreases to some extent during a strain burst (see SI and the above application of the analysis in Refs. [24,31]). A second is source unpinning: this was observed by Mompiou et al. [12] to occur via cross-slip of the fixed source arm and shown in simulations of Motz et al. [33] to occur by lock unzipping or reaction with other dislocations. Our DD simulations, in which pinning points remain fixed, and also the experimental data, give evidence of other mechanisms: in the larger samples explored here, displacement burst cessation can also be caused by events involving cross-slip of the moving arm and by lock formation. The importance of cross-slip is apparent in the data: Fig. 5d indicates that, as the resolved shear stress on the cross-slip plane increases, so does the propensity for burst cessation. Removing cross-slip from the code with all else unchanged increases significantly the amplitude of displacement bursts, Fig. 3d (note also that the long burst in Fig. 3d ended on its own: cross-slip aids burst cessation but is not a necessary condition). Essentially removing cross-slip and lock formation was also produced experimentally, by casting and testing a few microcast wires of pure magnesium; see the SI. In microcast magnesium wires oriented for glide along the basal plane slip, once initiated, only stops once the basal plane has rotated so far off its initial orientation that the resolved shear stress has strongly decreased, turning deformed cylindrical magnesium wires into thin ribbons. Here slip proceeds by the propagation of a strongly slipped region, spreading along the wire length, unlike aluminium, where slip bursts start and stop stochastically along the wire length.

Looking in detail at sequential dislocation configurations extracted from the DD simulations gives hints as to how cross-slip of the moving arm drives source cessation. If one watches carefully the films (see SI), one notices that there are only a few pinning points around which an arm rotates consistently to generate a large localized displacement burst. Figure 5e shows a snapshot near one

such pinning point at the moment when its corresponding rotating dislocation arm (shown by the blue arrow in the snapshots) is just about to stop turning. Earlier, while turning, this arm cross-slipped many times: cross-slip of the turning arm thus did not *per se* cause cessation of the displacement burst. Rather, when motion of the arm suddenly stops, on the next frame (see Figure 5f), one notices that it now contains a short segment in the cross-slip plane shown by the green arrow in the snapshot. Similar events can be spotted elsewhere in the simulations (e.g., at $t = 43$ s in the same film, to the left of the pinning point on Fig. 5e (see SI)). This suggests that stochastic source blockage involves either (i) cross-slip driven within the complex stress landscape of the sample to generate only a portion of (blocking) cross-slipped arm along its length, or (ii) a combination of cross-slip and sessile lock formation by interaction of the source dislocation with forest dislocations.

Since cross-slip is a random stochastic event the mechanism proposed here rationalizes the exponential distribution of large displacement bursts. That the halting of single-arm-source operation can be connected with cross-slip then points to why larger slip burst statistics do not depend strongly on D: the probability for cross-slip increases with the length of the dislocation arm and with the applied stress, in roughly linear fashion. Now, the arm length scales as $\sim D$ and the stress scales as $\sim 1/D$, so that the product is approximately independent of D. A corollary is that, as D increases, with a relatively constant upper limit on burst amplitudes, serrations become increasingly less visible on stress-strain curves (see Eq. S-8 of the SI).

In conclusion, using a novel fabrication method to create long-length specimens over a range of diameters down to 6 μm, we find $1/D$ scaling and plasticity dominated by large displacement bursts having an exponential distribution, with distinct dependence on single vs. multiple slip. DD simulations show that the size scaling and bursts are associated with the operation of single-arm-sources, and that the cessation of source operation is linked with cross-slip. Macroscopic samples are unfortunately still beyond the limit of what large-scale DD simulations can currently tackle; however, once this becomes possible, experiment will accompany simulation step-by-step because metal

casting has crossed the bridge from micro to macro. This age-old process can indeed now produce samples seamlessly spanning the entire range from microcrystals up to the macroscopic single crystals that were grown and tested in the earliest studies of crystal plasticity.

Acknowledgements

Author contributions

Jérôme Krebs and Suzanne Verheyden performed the experiments and produced all the experimental data; Jérôme Krebs, Csilla Miko, Russell Goodall and Andreas Mortensen developed the microcasting process; Satish I. Rao and William A. Curtin conducted all the 3D dislocation dynamics simulations;

Jérôme Krebs, Satish I. Rao, William A. Curtin and Andreas Mortensen wrote the text; Jérôme Krebs, Suzanne Verheyden, Satish I. Rao, Russell Goodall and Andreas Mortensen produced figures; Satish I. Rao produced the films; Jérôme Krebs, Satish I. Rao, Suzanne Verheyden, William A. Curtin and Andreas Mortensen interpreted and discussed the results.

Competing financial interests

The authors declare no competing financial interests.

Data availability

For access to more detailed data than are given in the article or the supplementary on-line information please contact the authors.

References

1 – Kubin, L.P. *Dislocations, mesoscale simulations and plastic flow*, Oxford University Press, Oxford, UK, 307pp. (2013).

2 - Uchic, M.D. Shade, P.A. & Dimiduk D.M. Plasticity of micrometer -scale single crystals in compression, Annu.Rev.Mater.Res., **39**, 361-386 (2009).

3 – Greer J. R. & De Hosson J. T. M. Plasticity in small-sized metallic systems: Intrinsic versus extrinsic size effect, Prog. Mater. Sci., **56**, 654–724 (2011).

4 – Kraft, O. Gruber, P. A. Moenig, R. & Weygand D. Plasticity in Confined Dimensions, Annual Review of Materials Research, **40**, 293–317 (2010).

5 - Dehm, G. Miniaturized single-crystalline fcc metals deformed in tension: New insights in size-dependent plasticity, Progress in Materials Science **54**, 664-688 (2009).

6 - Weinberger, C.R. & Cai, W. Plasticity of metal nanowires, Journal of Materials Chemistry, **22**, 3277-3292 (2012).

7 - Huetsch, J. & Lilleodden, E. T. The influence of focused-ion beam preparation technique on microcompression investigations: Lathe vs. annular milling, Scr. Mater., **77**, 49–51 (2014).

8 - Volkert, C. A. & Minor, A. M. Focused ion beam microscopy and micromachining," MRS Bull., **32**, 389–395 (2007).

9 - Bei, H., Shim, S. Miller, M. K., Pharr, G. M. & George, E. P. Effects of focused ion beam milling on the nanomechanical behavior of a molybdenum-alloy single crystal, Appl. Phys. Lett., **91,** 111915 (2007).

10 - Kiener, D., Motz, C., Rester, M. Jenko, M. & Dehm, G. FIB damage of Cu and possible consequences for miniaturized mechanical tests Mater. Sci. Eng. -Struct. Mater. Prop. Microstruct. Process., **459**, 262–272 (2007).

11 - S. Shim, H. Bei, M. K. Miller, G. M. Pharr, and E. P. George, Effects of focused ion beam milling on the compressive behavior of directionally solidified micropillars and the nanoindentation response of an electropolished surface, Acta Materialia **57,** 503–510 (2009).

12 - Mompiou, F., Legros, M., Sedlmayr, A., Gionalo, D.S., Caillard, D. & Kraft, O., Source-based strengthening of sub-micrometer Al fibers, Acta Materialia **60**, 977-983 (2012).

13 – Johanns, K.E., Sedlmayr, A., Phani, P.S., Mönig, R., Kraft, O., George, E.P., and Pharr, G.M., In-situ tensile testing of single-crystal molybdenum alloy fibers with various dislocation densities in a scanning electron microscope, J. Materials Research, **27**, 508-520 (2012).

14- Chisholm, C., Bei, H., Lowry, M.B., Oh, J., Syed Asif, S.A., Warren O.L., Shan Z.W., George, E.P., Minor, A.M., Dislocation starvation and exhaustion hardening in Mo alloy nanofibers, Acta Materialia, **60**, no 5, 2258–2264, (2012).

15 - Rao, S.I., Dimiduk, D.M. , Parthasarathy, T.A., Uchic, M.D., Tang, M. & Woodward, C. Athermal mechanisms of size-dependent crystal flow gleaned from three-dimensional discrete dislocation simulations, Acta Materialia, **56**, 3245-3259 (2008).

16 - Baumeister, G.,Buqezi-Ahmeti, D., Glaser, J., & Ritzhaupt-Kleissl H.J. New approaches in microcasting: permanent mold casting and composite casting, Microsyst Technol, **17,** 289-300 (2011).

17 - Rögner, J., Lang, K.H., Baumeister, G. & Schulze, V. Microstructure and mechanical properties of micro tensile specimens made of CuAl10Ni5Fe4 produced by micro casting, Microsyst Technol., **17,** 301-311 (2011) .

18 - Tabata, T., Fujita, H., Yamamoto, S., Cyoji, T., Effect of specimen diameter on tensile behaviors of aluminum thin wires. J. Phys. Soc. Jpn., **40**, 792–797 (1976).

19 - Ng, K. S. & Ngan, A. H. W. Stochastic nature of plasticity of aluminum micro-pillars, Acta Materialia, **56,** 1712–1720 (2008).

20 - Rao, S.I., Dimiduk, D.M., El-Awady, J.A., Parthasarathy, T.A., Uchic, M.D. & Woodward C.,"Atomistic simulations of cross-slip nucleation at screw dislocation intersections in face-centered cubic nickel," Philosophical Magazine, **89**, 3351-3369 (2009).

21 - Hussein, A.M., Rao, S.I., Uchic, M.D., Dimiduk, D.M., & El-Awady, J.A. Microstructurally based cross-slip mechanisms and their effects on dislocation microstructure evolution in fcc crystals, Acta Materialia, **85**, 180-190 (2015).

22 - Dimiduk, D. M., Woodward, C., LeSar, R. & Uchic, M. D. Scale-free intermittent flow in crystal plasticity, Science, **312**, 1188–1190 (2006).

23 - Kiener, D., Grosinger, W. Dehm, G. &Pippan, R. A further step towards an understanding of size-dependent crystal plasticity: In situ tension experiments of miniaturized single-crystal copper samples, Acta Materialia, **56**, 580–592 (2008).

24 - Csikor, F. F., Motz, C., Weygand, D. Zaiser, M., & Zapperi S. , Dislocation avalanches, strain bursts, and the problem of plastic forming at the micrometer scale, Science, **318**, 251–254 (2007).

25 – Devincre, B. & Kubin, L., Scale transitions in crystal plasticity by dislocation dynamics simulations, Comptes Rendus de Physique, **11**, 274-284 (2010).

26 - T. Richeton, P. Dobron, F. Chmelik, J. Weiss, and F. Louchet, "On the critical character of plasticity in metallic single crystals," *Mater. Sci. Eng. A*, vol. 424, no. 1–2, pp. 190–195, May 2006.

27 - J. Weiss, T. Richeton, F. Louchet, F. Chmelik, P. Dobron, D. Entemeyer, M. Lebyodkin, T. Lebedkina, C. Fressengeas, and R. McDonald, "Evidence for universal intermittent crystal plasticity from acoustic emission and high-resolution extensometry experiments," *Phys. Rev. B*, vol. 76, no. 22, Dec. 2007.

28 - Zaiser, M., Moretti, P., Fluctuation phenomena in crystal plasticity - a continuum model. J. Stat. Mech.-Theory Exp. P08004. doi:10.1088/1742-5468/2005/08/P08004 (2005).

29 - Staubwasser, W., On work-hardening of aluminium-single crystals (99.99-percent) and its interpretation. Acta Metallurgica, **7**, 43–50 (1959).

30 - Kiener, D., Rester, M., Scheriau, S., Yang, B., Pippan, R., Dehm, G. Influence of external and internal length scale on the flow stress of copper. Int. J. Mater. Res. **98**, 1047–1053 (2007).

31 – Zaiser, M. and Nikitas, N., Slip avalanches in crystal plasticity: scaling of the avalanche cut-off, J. Stat. Mech.-Theory Exp. P04013 (2007).

32 – Dieter, G.E., *Mechanical Metallurgy,* Mc-Graw-Hill, Singapore, p. 128 (1988).

33 - Motz, C., Weygand, D., Senger, J. and Gumbsch, P., Initial dislocation structures in 3D-discrete dislocation dynamics and their influence on microscale plasticity, Acta Materialia, **57**, 1744-1754 (2009).

Methods

Casting aluminium microwires

The aluminium microcasting process that we have developed combines pressure infiltration processing with the production of single-crystalline NaCl moulds that have been grown around a pyrolizable organic micropattern; Figure 1 of the main text summmarizes the process. The NaCl crystals are grown similarly to what is practiced by amateur single-crystal growers (see for example http://www.waynesthisandthat.com/crystals.htm#single%20crystals), Fig. 1.a, namely by slow evaporation of saturated brine (≥99.8% purity sodium chloride NaCl, Sigma Aldrich, in distilled water). Large crystals are then obtained if one conducts the process slowly and in the absence of any vibration. The crystals nucleate on the bottom of the container and then, during their growth, embed the strings or fibres; we used nylon or carbon fibres, of diameter ranging from 100 to 6 μm. Some skill is needed to produce suitable crystals that can be pyrolized; in particular it is important to identify regions of the crystals that may contain trapped water and remove them by cleaving the NaCl crystals prior to pyrolysis. With suitable technique the end result is a single crystalline NaCl mould that espouses the shape of the former fibre and displays a surprisingly regular inner surface, as we show below.

Once produced and pyrolized, the moulds are filled with 99.99% aluminium using a gas-pressure infiltration apparatus; details of the infiltration procedure are given in the SI. This is followed by directional solidification from the bottom up, Fig. 1b. Finally the salt moulds are leached in a chromate-containing water solution (distilled water containing 0.84 g/l of $NaHCO_3$ and 1.62 g/l of Na_2CrO_4, corresponding to 0.01 mol concentrations of both $NaHCO_3$ and Na_2CrO_4) to gently release the tiny cast wires while protecting the aluminium from corrosion in water. Using the corrosion inhibitor reduces the thickness of oxide formed along the surface of aluminium after NaCl dissolution to a value below 10 nm; see Ref. [34].

Resulting microcast aluminium wires have a diameter between 6 and 100 μm, Fig.1.c-e, and a length typically ranging from 2 to 3 mm. X-ray diffraction shows that the aluminium wires are monocrystalline; this was verified for each sample reported here. Their crystallographic orientation is random in the sense that it cannot be pre-determined in the microcasting process; most likely, it is the chance orientation of whatever aluminium crystal first encountered the open cavity of the NaCl single-crystalline mould during metal solidification.

The as-cast wire surface roughness was investigated using atomic force microscopy (AFM). A few bumps, of maximum height around 80 nm, are present along their surface (perhaps residue coming from pattern pyrolysis); elsewhere, the root mean square roughness of the metal wire is ≈ 15 nm, which is similar to that of FIB milled specimens [30].

Tensile testing apparatus

The tensile test machine is composed of two main components, namely a moving stage and a force cell. The moving stage, onto which one end of the tensile specimen is glued, is controlled by a Maxon DC motor (Maxon number 118705; max 7250 rotation/min) coupled to a reduction gear (Maxon number 134785; reduction ratio: 3027:1). The rotational displacement of the motor is converted into a linear displacement using a micrometric screw device. The maximum travel distance of the moving stage is 20 mm. The motor is continuously piloted by a position-controller (Maxon EPOS 24/1) to a precision of 10 nm. With this set-up, the linear displacement rate of the moving stage can be set between 50 nm/s and 4000 nm/s. The moving stage displacement is recorded at a frequency of roughly 50 Hz.

Opposite to the moving stage, a removable load cell is fixed with a bolt. In each test, one of two Futek LPM200 load cells was used to measure the applied load on the wires; the load cell maximum force was 100 mN for wires of diameter below 50 μm and 500 mN for wires of diameter above

50 μm. According to the specifications given by the supplier, these load cells have a resolution of 0.3% of their respective nominal force at their nominal force. During the tests, the selected load cell was connected to a high-speed bridge module (NI-9237 from National instrument) that amplifies, samples (Analog to Digital Conversion), and buffers the signal. During the test, packets of 1000 measurement points (this being the buffer size) were continuously transferred to a computer, at a maximum rate of 50 kHz. This comparatively high sampling rate was chosen so as to be able to detect and measure the amplitude of recorded load drops (see below).

Displacement-force curves

The force-displacement signal recorded at roughly 50 Hz had a standard deviation of 0.012 mN and was used to plot the shear stress-shear strain flow curve of all tested samples. Raw data were processed by a home-written LabVIEW code using as input data the time-force-displacement data, the orientation of the wire previously determined using Laue diffraction (error: $\pm 2°$), the initial diameter of the wire measured from a SEM image taken prior to tensile testing (error: ± 0.1 μm), and the gauge length of the tested wire, as measured from an image taken using a binocular microscope (error: ± 10 μm).

Stress and strain values were then converted to values of projected shear stress (using the Schmid law) and strain (using Eq. 4.14 in [32]), assuming that the wires deform plastically by single slip along the system with the highest resolved stress. From these curves the critical resolved shear stress of each specimen was computed by measuring the resolved shear stress at 0.2% of plastic deformation (this flow stress value being somewhat arbitrary, we also computed the stress at the first load drop and the average of the stress at the onset of the first ten detected load drops, and found the same scaling of flow stress with wire diameter using those two alternate measures of yield stress).

Time-force data, recorded at a far higher frequency of 50 kHz, were used to investigate the statistics of intermittent displacement bursts that were found to characterize the plastic deformation of the microwires. To this end, a Labview code was written enabling the identification and measurement of the amplitude of individual displacement bursts; specifics are given in the Supplementary Information.

3D dislocation dynamics simulations

The dislocation dynamics simulations of this work are based on a code that was initially constructed to simulate the deformation of nickel micropillars, and adapted by adimensionalization to aluminium, for which it is suited given that both are face-centered metals of high stacking fault energy [35]. Two sizes, namely $20 \times 20 \times 50$ and $6 \times 6 \times 50$ μm^3, and three orientations of deformation, namely [111], [001] and [110] directions, were simulated. Samples were deformed under imposed uniaxial tension. The aspect ratios of these pillars are significantly smaller than that of microwires; however, the simulation domain length is sufficiently high that such domains may be considered as non-interacting with the remainder of the experimental sample. Hence simulation results, including the initial flow stress and strain-hardening behaviour, should be representative of the microwires.

Isotropic elasticity theory was used in the simulations (aluminium is nearly isotropic). The Poisson's ratio was set at 0.31. We used the three-dimensional well parallelized dislocation dynamics code, Paradis, developed at Lawrence Livermore National Laboratory [36], modified to include three distinct mechanisms of cross-slip of screw dislocations in fcc crystals discussed in the literature [15,20,21], namely surface cross-slip, intersection cross-slip, and jog (bulk) cross-slip. The cross-slip activation energies and activation volumes with respect to different stress components were obtained from the literature [15,20,21]. The temperature of the simulations was 300K. Cross-slip of screw dislocations was checked for every 5000 timesteps in the simulations and implemented in a stochastic fashion as described in the literature [19].

The sample was initially populated with Frank-Read Sources, placed randomly. The slip system of each Frank-Read source was chosen randomly among the 12 possible slip systems in fcc crystals. There were 576 Frank-Read sources of 20 μm size in the 20 μm samples and 172 Frank-Read sources of 6 μm size in the 6 μm samples, corresponding in both to an initial dislocation density of ~ 6×10^{11}/m^2. For the 6 μm case, some simulations were performed with 516 initial 6μm Frank-Read sources, which corresponded to an initial dislocation density of ~ 2×10^{12}/m^2 (see SI for specifics, notably Table S-2 for initial dislocation density distributions used in applying the analytical one-arm source model). The crystals were strained in tension along three multi-slip directions, namely [111], [001] and [110], at a constant strain rate of 10/s. Some 6 μm simulations were performed after adapting this deformation-controlled model to mimic load-control, as this is more representative of experimental conditions in this work: the stress was not allowed to drop and kept a constant whenever the plastic strain rate was greater than the applied strain rate of 10/s. Then, the stress was incremented only after the total strain at time t (elastic strain plus plastic strain) became less than 10t, where t is the time of deformation and 10 is the prescribed overall strain rate in the simulations.

References

34 - Diologent, F., Goodall, R. and Mortensen, A., Surface oxide in replicated microcellular aluminium and its influence on the plasticity size effect, *Acta Materialia*, **57**, 286–294 (2009).

35 - Murr., *L.E. Interfacial Phenomena in Metals and Alloys*, Addison-Wesley Publishers, Reading, MA (1975).

36 - Arsenlis, A., Cai, W., Tang, M. Rhee, M., Oppelstrup, T., Hommes, G. Pierce, T. G. & Bulatov, V.V., Enabling strain hardening simulations with dislocation dynamics, Modelling.Simul.Mater.Sci.Eng., **15**, 553-595 (2007).